



## Energy materials

# Bifunctional NiO@CoZnLDH composites with flower-like nanoarchitecture: synergistic enhancement of energy storage and water electrolysis performance

Ming-Xia Wang<sup>1</sup>, Xingming Zhao<sup>1,\*</sup> Dong-Mei Ma<sup>1</sup>, Yi Jia<sup>2</sup>, Hong-Sheng Chu<sup>1</sup>, Xiao-Ming Lu<sup>1</sup>, Jun Xiang<sup>1</sup>, Rongda Zhao<sup>1</sup>, and Fu-Fa Wu<sup>3</sup>

<sup>1</sup> School of Materials Science and Engineering, Liaoning University of Technology, 121001 Jinzhou, People's Republic of China

<sup>2</sup> School of Chemical and Environmental Engineering, Liaoning University of Technology, 121001 Jinzhou, People's Republic of China

<sup>3</sup> College of Materials Science and Engineering, Liaoning Technical University, 125105 Huludao, People's Republic of China

Received: 8 July 2025

Accepted: 27 August 2025

Published online:

14 September 2025

© The Author(s), under exclusive licence to Springer Science+Business Media, LLC, part of Springer Nature, 2025

## ABSTRACT

The development of high-performance energy materials is essential for addressing global energy challenges. In this study, a NiO@CoZnLDH composite electrode was synthesized via a two-step hydrothermal process, and its electrochemical performance was evaluated for applications in both supercapacitors and water electrolysis. The asymmetric supercapacitor (NiO@CoZnLDH//AC) achieved an energy density of 9.44 Wh/kg at a power density of 1132 W/kg, maintaining 73.6% of its capacitance after 8000 charge–discharge cycles. For electrocatalysis, the composite exhibits low overpotential for hydrogen evolution reaction and oxygen evolution reaction (188.8 and 322.2 mV at 10 mA/cm<sup>2</sup>) and enables stable overall water splitting at 1.84 V for 12 h in 1 M KOH. These results confirm that NiO@CoZnLDH is a promising bifunctional material for energy storage and conversion applications.

## Introduction

With the rapid growth in global energy demand, renewable energy technologies—particularly secondary batteries and supercapacitors—have attracted significant attention [1–3]. Among these, supercapacitors stand out due to their exceptional characteristics, including ultra-fast charging/discharging rates, high

power density, operational safety, low maintenance requirements, and long cycle life [4, 5]. As a result, they have been widely adopted in applications such as smartphones, smart grids, and electric generator systems [6, 7]. Supercapacitors are generally categorized into three types: electric double-layer capacitors (EDLCs), pseudocapacitors, and hybrid capacitors. EDLCs store energy via electrostatic charge separation

Handling Editor: Ivo Teixeira.

Address correspondence to E-mail: clzxm@lnut.edu.cn

E-mail Addresses: dmma@lnut.edu.cn; ffwu@lnut.edu.cn

<https://doi.org/10.1007/s10853-025-11455-8>

at the electrode–electrolyte interface, whereas pseudocapacitors rely on fast, reversible surface redox reactions for energy storage. Hybrid capacitors, which combine EDLC electrodes with pseudocapacitive materials, offer an optimal balance between energy density and power performance [8–10]. Hydrogen energy, characterized by its high energy density and clean feature, represents a sustainable solution to escalating energy demands [11, 12]. Producing hydrogen through hydrogen evolution reaction (HER) and oxygen evolution reaction (OER) is an environmentally friendly method that can effectively integrate renewable energy sources [13]. Leveraging supercapacitor electrode materials in water electrolysis systems enables multifunctional electrode performance across varied operational environments.

Among various energy storage and catalytic materials, conductive polymers, transition metal oxides, and activated carbon (AC) have found widespread application. Conductive polymers—such as polyaniline, polypyrrole, and polythiophene—exhibit high pseudocapacitance, excellent electrical conductivity, and processing versatility; however, their practical application is constrained by limited cycling stability. AC known for its ultra-high specific surface area and outstanding cycle life, is hindered by relatively low specific capacitance and energy density. In contrast, transition metal oxides offer superior specific capacitance and energy density [14, 15], making them promising electrode materials for hybrid capacitors. Notable examples include manganese-, cobalt-, and nickel-based compounds, with nickel oxide (NiO) standing out due to its non-toxicity, low cost, chemical and thermal stability, and ease of synthesis [16, 17]. Furthermore, NiO's high theoretical specific capacitance has attracted significant attention for its potential in supercapacitor applications [18, 19].

Recent advancements in NiO-based materials include studies such as that of Muhammad et al., who synthesized a TiO<sub>2</sub>/NiO/ZnO ternary core–shell array (TCSA) via an ex-situ method, which was used as a battery-supercapacitor hybrid system (BSCH). This material achieved performances of 3350 W/kg and 43.9 Wh/kg at 1.5 V, accompanied by acceptable cycle durability [20]. Similarly, Yin et al. fabricated NiO/CuO heterostructured nanosheets on nickel foam (NiO/CuO/Ni foam) for electrocatalytic oxygen evolution, demonstrating enhanced OER activity with an overpotential of 234 mV at a current density of 10 mA/cm<sup>2</sup> and a Tafel slope of 22 mV/dec [21]. These findings

collectively highlight the dual functionality of NiO-based materials in both energy storage and water electrolysis applications [22].

Layered double hydroxides (LDHs) with transition metal compounds can regulate the electronic structure and morphology of the interface, thereby increasing the OER kinetics [12, 23–25]. Among various compositions, ZnCo-LDHs demonstrate superior OER electrocatalytic performance compared with non-precious metal catalysts [26, 27], positioning them as promising materials for energy conversion technologies. For example, the 3D heterostructured NiSe@CoFe-LDH nanoarrays synthesized on Ni foam (NiSe@CoFe-LDH/NF) by Nie et al. have a very low OER overpotential under alkaline conditions (203 mV/236 mV at 10 mA/cm<sup>2</sup> and 100 mA/cm<sup>2</sup>) and can still operate stably for over 80 h at 100 mA/cm<sup>2</sup> [28]. Zhu et al. demonstrated another breakthrough with CNT@NiCo-LDH hybrid electrodes, which exhibited remarkable electrochemical performance [29]. The assembled asymmetric supercapacitor (ASC) employing CNTs@NiCo-LDH//ZIF-8-derived carbon exhibited a high energy density of 37.38 Wh/kg at a power density of 800 W/kg, along with 90.22% capacitance retention after 5200 cycles. These case studies collectively affirm the versatility of LDH-based materials in both supercapacitor and water electrolysis systems.

Building upon the aforementioned advancements in energy storage and conversion materials, this study introduces a strategically designed NiO@CoZnLDH composite electrode fabricated through a two-step hydrothermal process. Leveraging the synergistic interaction between the robust pseudocapacitive behavior of NiO and intrinsic electrocatalytic activity of CoZn-layered double hydroxide (LDH), the resulting hierarchical architecture demonstrates remarkable bifunctional electrochemical performance. In supercapacitor configurations, the assembled NiO@CoZnLDH//AC asymmetric device delivers an energy density of 9.44 Wh/kg at a power density of 1132 W/kg, retaining 73.6% of its capacitance after 8000 cycles—a durability metric essential for commercial viability. For electrolysis applications, the overpotentials for the hydrogen evolution reaction and the oxygen evolution reaction of this composite material were 188.8–322.2 mV at 10 mA/cm<sup>2</sup>, and stable operation was sustained during the 12 h overall water splitting tests. These findings not only validate the effectiveness of material hybridization strategies but also establish NiO@CoZnLDH as a versatile platform technology

for integrated energy systems requiring concurrent energy storage and conversion functionalities.

## Experiments

The analytical reagents  $\text{Ni}(\text{NO}_3)_2 \cdot 6\text{H}_2\text{O}$ ,  $\text{Co}(\text{NO}_3)_2 \cdot 6\text{H}_2\text{O}$ ,  $\text{NH}_4\text{F}$ ,  $\text{Zn}(\text{NO}_3)_2 \cdot 6\text{H}_2\text{O}$ , and  $\text{CO}(\text{NH}_2)_2$  were utilized as reactants. Nickel foam (Ni Foam) was selected as the electrode material. A  $\text{NiO}@\text{CoZnLDH}$  composite was successfully synthesized via a scalable two-step hydrothermal method. Firstly, nickel foam ( $3 \times 4 \times 0.15 \text{ cm}^2$ ) was immersed in 1 mol/L dilute hydrochloric acid for 30 min, then transferred to deionized water for ultrasonic cleaning for 1 h. It was placed in a 60 °C oven for drying for 6 h to remove impurities on the surface of the nickel foam. In a 100 ml high-pressure reaction kettle, 1.5 mmol of nickel nitrate hexahydrate ( $\text{Ni}(\text{NO}_3)_2 \cdot 6\text{H}_2\text{O}$ ), 5 mmol of urea and 2.5 mmol of ammonium fluoride ( $\text{NH}_4\text{F}$ ) were added, followed by 50 ml of deionized water. The solution was stirred with a magnetic stirrer for 40 min. The above-treated nickel foam was added, and the high-pressure reaction kettle was placed in a 120 °C oven for reaction for 8 h. As a result, samples were repeatedly washed with deionized water and anhydrous ethanol, and then dried at 60 °C for 6 h to obtain  $\text{NiO}$  samples.

Secondly, 1 mmol of  $\text{Co}(\text{NO}_3)_2 \cdot 6\text{H}_2\text{O}$ , 1 mmol of  $\text{Zn}(\text{NO}_3)_2 \cdot 6\text{H}_2\text{O}$ , 1 mmol of urea, 1 mmol of  $\text{NH}_4\text{F}$ , and 50 ml of deionized water were weighed and placed

in a 100 ml high-pressure reactor. It was stirred in a magnetic stirrer for 40 min.  $\text{NiO}$ /nickel foam was added, and the autoclave was placed in an oven at 120 °C for 3 h. After the reaction, it was thoroughly rinsed with deionized water and anhydrous ethanol alternately, followed by drying at 60 °C for 6 h. The average loading masses of  $\text{NiO}$ ,  $\text{CoZnLDH}$ , and the  $\text{NiO}@\text{CoZnLDH}$  electrode were  $1.11 \text{ mg/cm}^2$ ,  $0.94 \text{ mg/cm}^2$ , and  $1.46 \text{ mg/cm}^2$ , respectively. The  $\text{NiO}@\text{CoZnLDH}$  is illustrated in Fig. 1.

The samples were analyzed by X-ray diffraction (XRD, D/max-2500/PC, Cu K $\alpha$  radiation), with the diffraction angle range from 10 to 90°, tube voltage of 40 kV, and scanning rate of 8°/min. The surface chemical element composition and valence state of the samples were detected by X-ray photoelectron spectroscopy (XPS, ESCALAB250). The microstructure and morphology of the materials were studied using a ZeissSigma 500 scanning electron microscope (SEM, output voltage of 15 kV, current ranging from 3 to 20 mA, low vacuum range of 2–133 Pa) and energy dispersive X-ray spectroscopy (EDS). The Brunner-Emmet-Teller (BET, SSA-7000) measurement was employed to analyze the specific surface area and porosity of the samples. Table S1 shows all the abbreviations used in the study.

Using the Chi760e electrochemical workstation in a standard three-electrode system, a sample with a diameter of 1 cm was used as the working electrode,  $\text{Hg}/\text{HgO}$  as the reference electrode, and a platinum electrode as the counter electrode. The cyclic

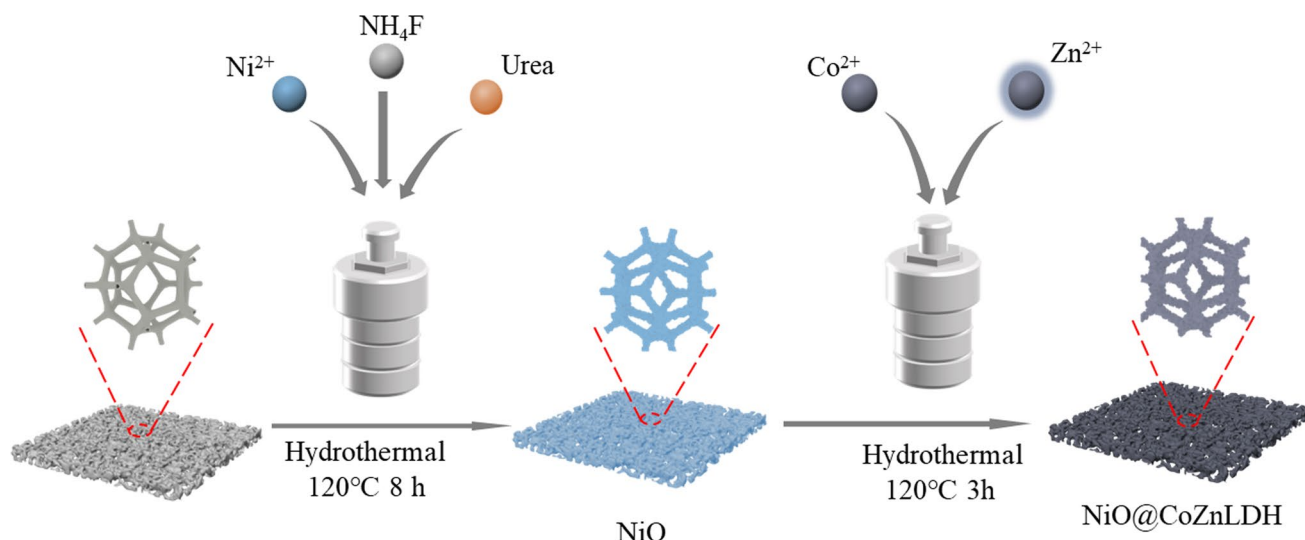


**Figure 1** Diagram of the process for preparing  $\text{NiO}@\text{CoZnLDH}$  by hydrothermal method.

voltammetry (CV), galvanostatic charge–discharge (GCD), and EIS methods were employed to study the electrode performance in a 3 M KOH electrolyte solution. The scanning voltage of CV test was 0 ~ 0.6 V, and the scanning rate was 5 ~ 100 mV / s. The EIS test frequency range is 100 k Hz ~ 0.1 Hz. The sample area of  $0.5 \times 0.5 \text{ cm}^2$  was used as the working electrode, Hg/HgO was used as the reference electrode, and the carbon rod was used as the counter electrode. The electrocatalytic performance of the samples was studied by CV, linear sweep voltammetry (LSV) and *i-t* curve in 1 M KOH electrolyte solution. GCD curve tests were conducted at a 1–10 A/g current density within the 0–0.5 V potential range. The energy density (E) and power density (P) were obtained through formulas (1) and (2)[30]:

$$E = \frac{C(\Delta V)^2}{2 \times 3.6} \quad (1)$$

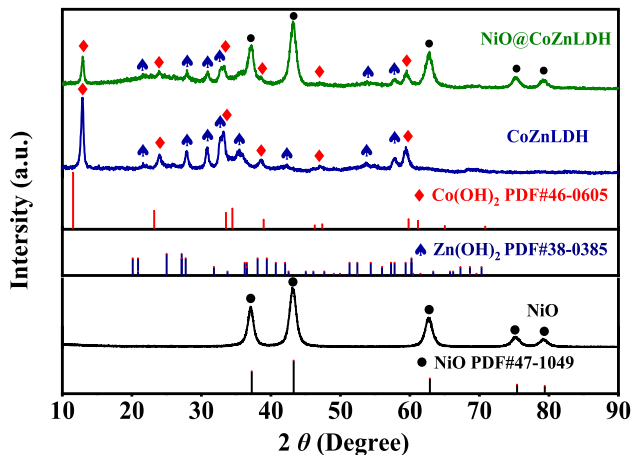
$$P = \frac{3600E}{\Delta t} \quad (2)$$

Table S1 All the abbreviations used in the study.

## Results and discussion

The crystal structures of NiO, CoZnLDH, and NiO@CoZnLDH electrode materials were analyzed by XRD data, as illustrated in Fig. 2. For the NiO, the diffraction peaks at  $2\theta$  angles of  $37.08^\circ$ ,  $43.24^\circ$ ,  $62.88^\circ$ ,  $75.20^\circ$ , and  $79.32^\circ$  correspond to the (111), (200), (220), (311), and (222) crystal planes of NiO (PDF#47–1049), respectively. In the CoZnLDH, peaks observed at  $2\theta$  angles of  $21.70^\circ$ ,  $27.92^\circ$ ,  $30.90^\circ$ ,  $32.98^\circ$ ,  $53.86^\circ$ , and  $57.88^\circ$  (marked with peach blossom symbols) are indexed to the (110), (101), (211), (002), (312), and (131) crystal planes of Zn(OH)<sub>2</sub> in CoZnLDH (PDF#38–0385). Similarly, the red diamond-shaped peaks at  $2\theta$  angles of  $12.92^\circ$ ,  $23.96^\circ$ ,  $33.18^\circ$ ,  $38.62^\circ$ ,  $46.98^\circ$ , and  $59.42^\circ$  correspond to the (003), (006), (100), (105), (108), and (110) crystal planes of Co(OH)<sub>2</sub> in CoZnLDH (PDF#46–0605). Notably, the diffraction peaks of the NiO@CoZnLDH align precisely with those of the precursor materials, confirming the successful growth of CoZnLDH on the NiO substrate and the successful preparation of the NiO@CoZnLDH composite.

The elemental valence states and extranuclear electronic energy changes of the NiO@CoZnLDH



**Figure 2** XRD patterns of the NiO@CoZnLDH, CoZnLDH and NiO electrode materials from top to bottom.

composite were analyzed using XPS, and the results are shown in Figure 3. Fig. 3a presents the survey spectrum, confirming the presence of Ni, O, Zn, and Co in the composite. In the Ni 2p spectrum (Fig. 3b), the main peaks corresponding to NiO appear at binding energies of 855.8–873.6 eV, accompanied by satellite peaks at 861–880 eV, respectively. The peaks at 855.8–861 eV are attributed to Ni 2p<sub>3/2</sub>, while those at 873.6–880 eV correspond to Ni 2p<sub>1/2</sub>, confirming the presence of Ni<sup>2+</sup> species [31]. Additionally, compared to the NiO substrate, the oxidation state peaks of the NiO@CoZnLDH composite electrode exhibit a noticeable shift of about 0.3 eV in the negative direction, indicating electronic interaction between the extranuclear electrons of CoZnLDH and those of the NiO substrate.

The O 1 s spectrum (Fig. 3c) of the NiO substrate primarily shows contributions from metal–oxygen bonds and OH<sup>-</sup> ions from adsorbed water. After CoZnLDH composite formation, the O 1 s spectrum of NiO@CoZnLDH resolved into three distinct components: lattice metal–oxygen bonds, Zn–O bonds, and Co–O bonds. The lattice metal–oxygen bond peak exhibited a positive binding energy shift (approximately 0.4 eV), confirming successful CoZnLDH integration with the NiO matrix [32]. In the Co 2p spectrum (Fig. 3d), the primary peaks appear at binding energies of 781.2–797.3 eV, accompanied by satellite peaks at 785.7–804.1 eV, respectively. The peaks at 781.2–785.7 eV correspond to Co 2p<sub>3/2</sub>, while those at 797.3–804.1 eV are attributed to Co 2p<sub>1/2</sub>, indicating the presence of both Co<sup>2+</sup> and Co<sup>3+</sup> ions [32]. The Zn 2p spectrum (Fig. 3e) displays symmetric Zn<sup>2+</sup> peaks

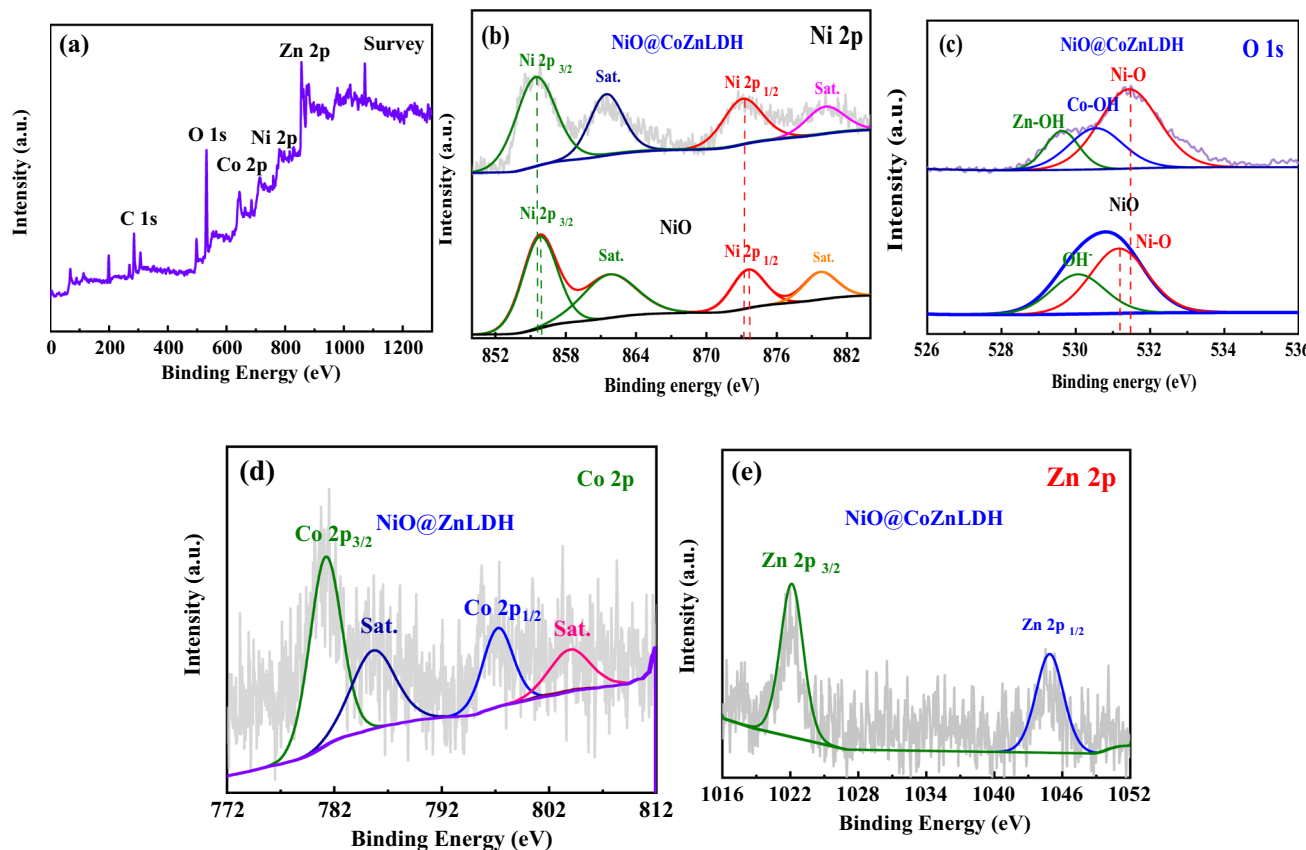


**Figure 3** **a** Full scan spectrum, **b** XPS spectra of Ni 2p, **c** XPS spectra of O 1 s, **d** XPS spectra of Co 2p, **e** XPS spectra of Zn 2p.

at 1021.8 eV (Zn 2p<sub>3/2</sub>) and 1044.9 eV (Zn 2p<sub>1/2</sub>), consistent with previously reported Zn<sup>2+</sup> valence states in layered double hydroxides [32]. These combined spectroscopic results confirm the successful fabrication of the NiO@CoZnLDH composite material with well-defined electronic interactions at the heterointerface.

The morphology of the NiO@CoZnLDH composite was examined using SEM. As shown in Fig. 4a, b, NiO exhibits a flake-like structure, suggesting a large specific surface area conducive to hosting active materials. Fig. 4c, d illustrate the NiO@CoZnLDH composite, where flower-like CoZnLDH nanoparticles are uniformly grown on the flaky NiO substrate. This hierarchical architecture not only increases the density of active sites but also enhances electrochemical stability. Moreover, the intimate interface between CoZnLDH and NiO facilitates efficient charge transfer, synergistically enhancing the composite's performance in electrochemical energy storage and water electrolysis. Fig. 4e presents the EDS mapping of NiO@CoZnLDH. Notably, the Ni signal from the NiO substrate is completely masked

by the Co and Zn signals at the CoZnLDH growth sites, confirming successful deposition of CoZnLDH onto NiO and indicating high crystallinity of the composite.

Nitrogen adsorption–desorption isotherms and pore size distribution analyses were conducted to evaluate the specific surface area and porosity of the samples, as shown in Figs. 4f, g. Both CoZnLDH and NiO@CoZnLDH exhibit classic type IV isotherms with H3 hysteresis loops [33], indicative of mesoporous structures. The BET-specific surface areas and BJH pore diameters were calculated for each sample. CoZnLDH exhibited a specific surface area of 8.189 m<sup>2</sup>/g and a pore diameter of 20.94 nm; NiO showed a specific surface area of 8.156 m<sup>2</sup>/g and a pore diameter of 10.92 nm. Notably, the NiO@CoZnLDH electrode displayed a significantly higher specific surface area of 62.872 m<sup>2</sup>/g and a reduced pore diameter of 13.94 nm. These results indicate that the integration of NiO and CoZnLDH leads to a marked increase in surface area, providing abundant charge storage and active sites for water-splitting reactions, thereby enhancing both

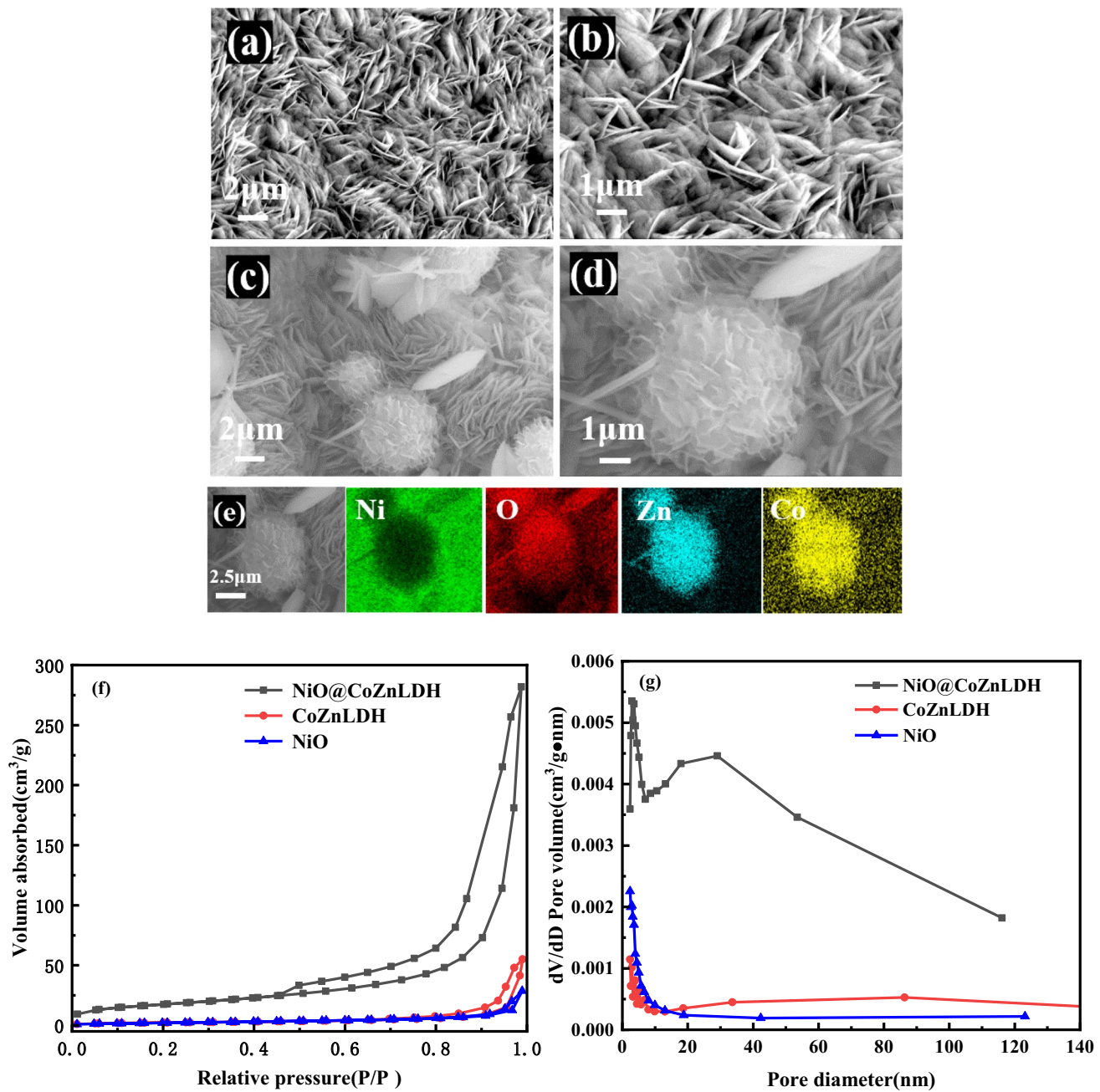


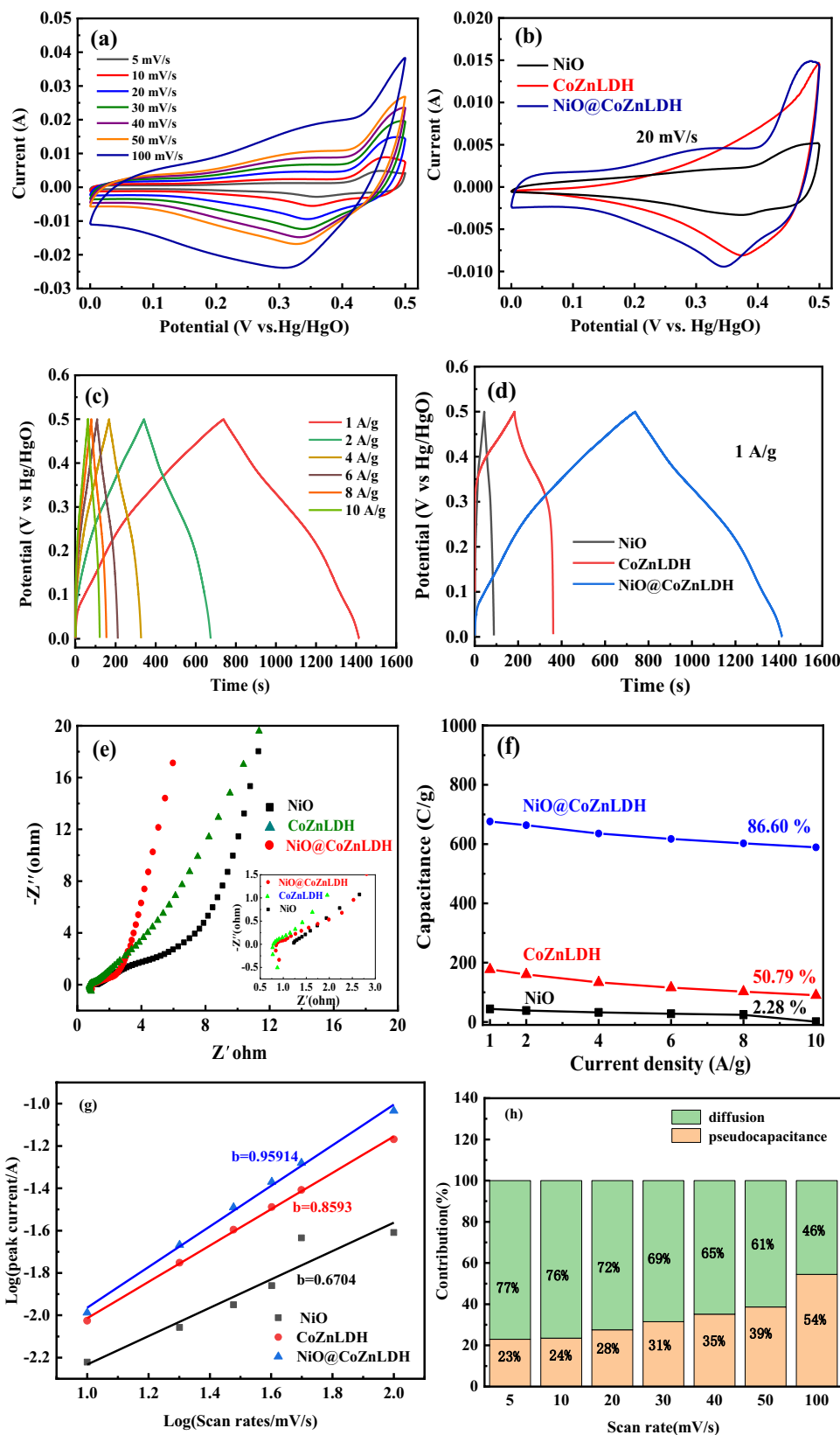
**Figure 4** **a–b** SEM of NiO; **c–d** SEM of NiO@CoZnLDH; **e** EDS mapping of NiO@CoZnLDH; **f**  $N_2$  adsorption–desorption isotherms; **g** pore size distribution of CoZnLDH and NiO@CoZnLDH composite.

energy storage and hydrogen evolution performance during water electrolysis.

Figure 5a shows the CV curves of NiO@CoZnLDH at scan rates ranging from 5 to 100 mV/s. Notably, as the scanning rate increases, the area enclosed by the curve in the CV graph also increases accordingly, while no morphological degradation is observed,

suggesting excellent capacitance retention and rate capability. Furthermore, the oxidation and reduction peaks shift to higher and lower potentials, respectively, with increasing scan rate, confirming the polarization behavior of the NiO@CoZnLDH electrode. Fig. 5b shows the CV curves of NiO, CoZnLDH and NiO@CoZnLDH at a scanning rate of

**Figure 5** **a** CV curves of the NiO@CoZnLDH at 5–100 mV/s; **b** CV curves of NiO, CoZnLDH and NiO@CoZnLDH at 20 mV/s; **c** GCD curves of the NiO@CoZnLDH at 1–10 A/g; **d** GCD curves of NiO, CoZnLDH and NiO@CoZnLDH at 1 A/g; **e** EIS curves of NiO, CoZnLDH and NiO@CoZnLDH; **f** Specific capacitance curve of NiO, CoZnLDH and NiO@CoZnLDH; **g** **h** value of NiO, CoZnLDH and NiO@CoZnLDH; **h** contribution ratios of pseudocapacitance and diffusion-controlled capacitance of NiO@CoZnLDH at different scanning rates.



20 mV/s. The CV curve of NiO@CoZnLDH shows a substantially larger enclosed area than those of NiO and CoZnLDH, with peak potentials shifting to higher oxidation potentials and lower reduction potentials. This observation confirms the enhanced polarization and superior electrochemical activity of the composite electrode, which is consistent with its improved performance.

Figure 5c–d present the GCD profiles of the NiO@CoZnLDH electrode at current densities ranging from 1 to 10 A/g, alongside comparisons with NiO, CoZnLDH, and a blank reference electrode at 1 A/g. Remarkably, the GCD profiles of NiO@CoZnLDH maintain nearly identical shapes across all the current densities, indicating stable electrochemical reversibility. At 1 A/g, the discharge time reaches 1415.6 s, corresponding to a mass-specific capacitance of 676.7 C/g, which is about 15.4 times greater than that of NiO (43.9 C/g) and about 3.8 times greater than that of CoZnLDH (177.4 C/g). This result unequivocally demonstrates the synergistic enhancement of the composite structure. To investigate the impedance characteristics, EIS was performed. As shown in Fig. 5e, the Nyquist plot of NiO@CoZnLDH exhibits the smallest semicircle diameter (indicating minimal charge-transfer resistance) and the steepest low-frequency slope (suggesting rapid ionic diffusion), outperforming those of NiO and CoZnLDH. Notably, NiO@CoZnLDH demonstrates the lowest equivalent series resistance (ESR) at identical current densities, which aligns with its enhanced capacitance. Figure 5f shows the mass-specific capacitances of the three materials, clearly demonstrating the significant improvement in the specific capacitance of NiO@CoZnLDH after CoZnLDH was compounded onto the NiO substrate. To elucidate the energy storage mechanisms, the capacitive contribution was quantified using Eq. (3), which provides quantitative insights into the charge storage behavior of the electrodes [34]:

$$i = av^b \quad (3)$$

In the given formula,  $a$  and  $b$  are constant parameters. When the value of  $b$  lies between 0.5 and 1, the system is categorized as a pseudocapacitor-battery hybrid. As illustrated in Fig. 5g, the calculated  $b$ -values for NiO, CoZnLDH, and NiO@CoZnLDH are 0.67, 0.86, and 0.96, respectively. These results suggest that the devices incorporating these

electrode materials as the positive electrode exhibit hybrid energy storage behavior. Fig. 5h shows the ratio of capacitance and diffusion-controlled charge storage of NiO@CoZnLDH as a function of the scan rate. As the scan rate increases from 10 to 100 mV/s, the influence of diffusion control decreases, while the influence of capacitance control becomes more pronounced. These results indicate that a substantial number of hydroxide ions are being inserted into the NiO@CoZnLDH electrode, leading to a higher capacitance. However, most redox reactions tend to take place at the near surface region of the NiO@CoZnLDH active material as the current density increases. Furthermore, these findings indicate that at higher current densities, the charge storage mechanism shifts to a surface capacitance process, where most of the charge storage occurs at the interface between electrode and electrolyte.

To further investigate the supercapacitor performance of the NiO@CoZnLDH electrode, we constructed an asymmetric supercapacitor device (NiO@CoZnLDH//AC), where NiO@CoZnLDH served as the positive electrode, AC served as the negative electrode, and polyvinyl alcohol-potassium hydroxide (PVA-KOH) gel was used as the electrolyte ( $\text{PH} = 14$ ). The electrochemical performance was systematically evaluated. Fig. 6a, b show the CV curves of the NiO@CoZnLDH//AC device at 100 mV/s under different voltage windows and different scan rates. The enclosed area of the CV curves progressively increases with increasing scan rates or expanded voltage windows, indicating excellent rate capability and stable operation within the 0–1.5 V voltage range.

Figure 6c displays the GCD profiles, showing a specific capacitance of 30 C/g at a current density of 1 A/g, with the discharge curves maintaining their shape even at higher current densities. Fig. 6d presents the EIS curve of the NiO@CoZnLDH//AC device. The Nyquist plot displays a semicircle in the high-frequency region, corresponding to the charge transfer resistance ( $R_{\text{ct}}$ ). The EIS data were fitted to an appropriate equivalent circuit model (also shown in Fig. 6d), yielding values for  $R_{\text{ct}}$  and  $R_s$  (internal/bulk resistance). The fitted circuit parameters are summarized in Table S2, with all associated error rates below 10%. The close agreement between the fitted impedance spectrum and the experimental data confirms the physical validity of the equivalent circuit model.

Figure 6e illustrates the energy-power relationship in a Ragone plot, demonstrating that the device

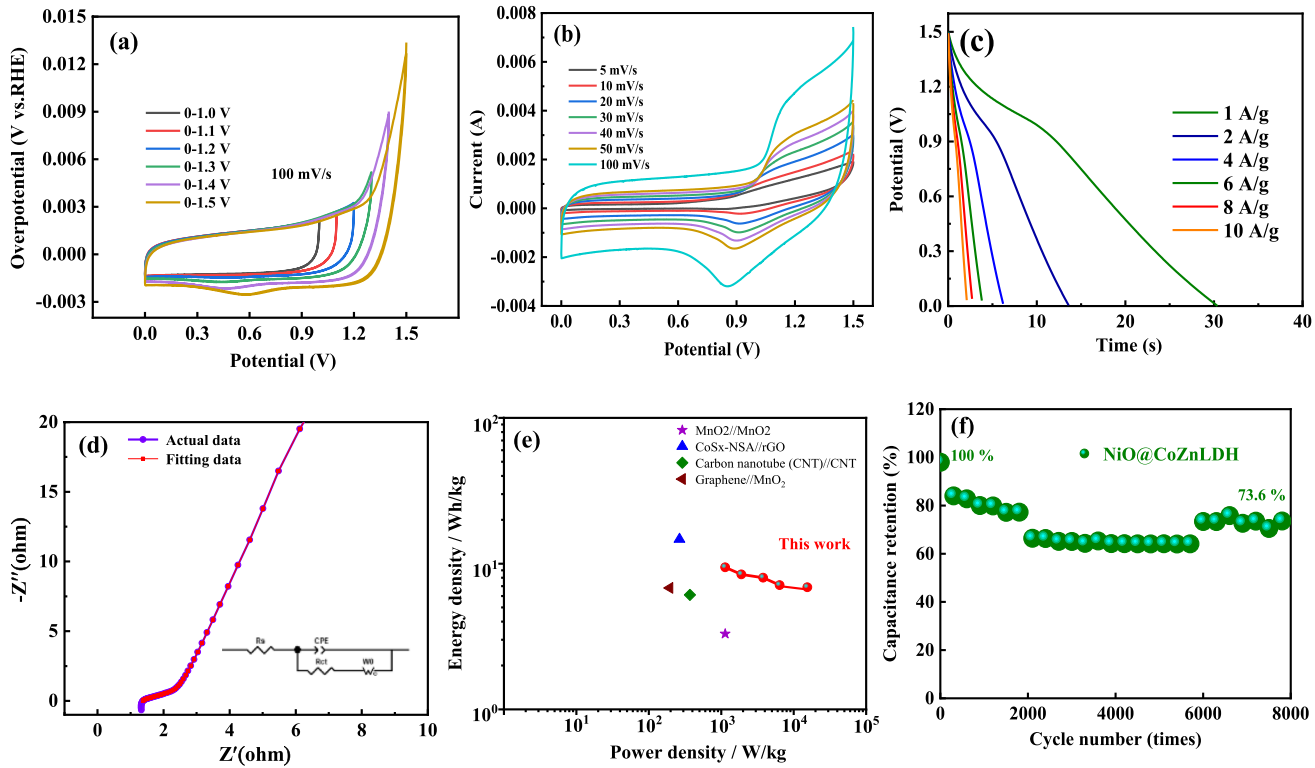


**Figure 6** Supercapacitor performance of the NiO@CoZnLDH//AC device **a** CV curves at different voltage windows; **b** CV curves at different scan rates; **c** GCD curves at different current density; **d** EIS curves; **e** Ragone plots; **f** cycling stability.

delivers a high power density of 1132 W/kg while retaining an energy density of 9.44 Wh/kg. These performance metrics surpass those reported in previous studies [35–38]. Finally, as shown in Fig. 6f, the cycling stability was evaluated over 8000 charge–discharge cycles at a current density of 20 mA/cm<sup>2</sup>. The device retained 73.6% of its initial capacitance, confirming excellent long-term durability.

In the three-electrode system, the HER and OER performance of the NiO@CoZnLDH electrode material, as well as the overall water splitting efficiency in the two-electrode system, were evaluated. The electrolyte used was a 1 M KOH solution. Initially, the HER performance of the electrode material was tested. To investigate the overpotential characteristics of water electrolysis at specific current densities, LSV curves were measured for the HER. As shown in Fig. 7a, the

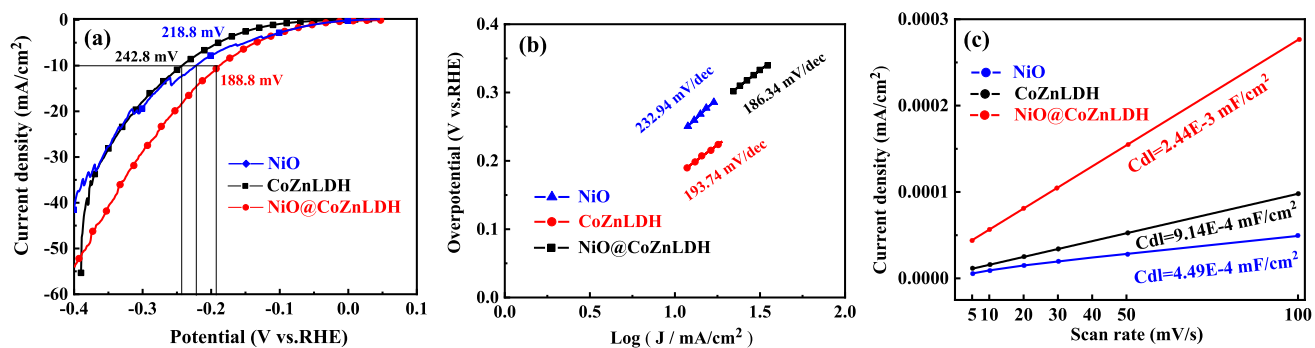


**Figure 7** HER performance of NiO, CoZnLDH, NiO@CoZnLDH **a** Comparison of LSV curve; **b** Comparison of Tafel slope; **c** Comparison of C<sub>dl</sub> curves.

NiO@CoZnLDH electrocatalyst exhibited an overpotential of 188.8 mV at 10 mA/cm<sup>2</sup>, which was significantly lower than those of pristine NiO and CoZnLDH, indicating superior hydrogen evolution performance for the NiO@CoZnLDH system. Tafel plots were subsequently constructed (Fig. 7b) to further analyze the differences in the reaction kinetics between the materials and the electrolyte. The NiO@CoZnLDH electrode demonstrated a Tafel slope of 186.34 mV/s, which was markedly lower than those of NiO (232.94 mV/dec) and CoZnLDH (193.74 mV/s), confirming its enhanced reaction kinetics. To evaluate the electrochemically active surface area (ECSA) and active site density, CV curves at various scan rates were linearly fitted to derive the double-layer capacitance(Cdl) (Fig. 7c). Compared with both the NiO and CoZnLDH electrodes, the NiO@CoZnLDH electrocatalyst presented the highest Cdl value ( $2.44 \times 10^{-3}$  mF/cm<sup>2</sup>), suggesting superior electric double-layer capacitance and active site density.

The OER activity of the NiO@CoZnLDH electrode material was systematically studied. As demonstrated in Fig. 8a, at a current density of 10 mA/cm<sup>2</sup>, the OER overpotential of the NiO@CoZnLDH electrocatalyst was 322.2 mV, which is lower than those of the NiO electrode (427.2 mV) and CoZnLDH electrode (406.2 mV). These findings indicate that the NiO@CoZnLDH composite electrocatalyst has superior performance compared with that of the precursor materials. Fig. 8b shows the Tafel slopes of the three electrocatalysts, revealing that the reaction kinetic characteristics of the OER in this system align with the trends observed in the HER. Notably, the NiO@CoZnLDH composite electrode exhibits the lowest Tafel slope value of 55.66 mV/dec, indicating

enhanced electrocatalytic activity. This superior performance can be attributed to several factors: (1) the layered structure of CoZnLDH provides a high density of exposed active sites, significantly increasing the electrode–electrolyte contact area; (2) the strong ionic activity of Co<sup>2+</sup> and Zn<sup>2+</sup> facilitates efficient charge transfer; and (3) the growth of CoZnLDH on the NiO substrate results in a composite material with faster charge transfer kinetics than the individual precursors, thereby improving water dissociation efficiency [32]. Compared with previously reported,

**Table 1** Comparison of HER performance of NiO@CoZnLDH electrocatalyst with other systems of catalysts

Materials	Overpotential (mV)	Electrolyte	Tafel plot (mV dec <sup>-1</sup> )	Refs.
AVL-CuO-ZrO <sub>2</sub>	225	1 M KOH	143	[40]
Fe <sub>3</sub> O <sub>4</sub> @pCoNi/fCoNi	290	1 M KOH	86	[41]
CuCo <sub>2</sub> O <sub>4</sub> @CQDs	331	1 M KOH	65	[42]
CoS <sub>x</sub> /Ni <sub>3</sub> S <sub>2</sub> @NF	204	1 M KOH	113	[43]
NiMoO <sub>4</sub> @CoMoO <sub>4</sub>	220	1 M KOH	142	[44]
Co-NRCNTs	370	1 M KOH	69	[45]
Au <sub>8.0</sub> @C/Co <sub>3</sub> O <sub>4</sub>	487	1 M KOH	76.1	[46]
CuCo <sub>2</sub> S <sub>4</sub> /carbon cloth	204	1 M KOH	50	[47]
NiO@CoZnLDH	188.8	1 M KOH	186.34	This work

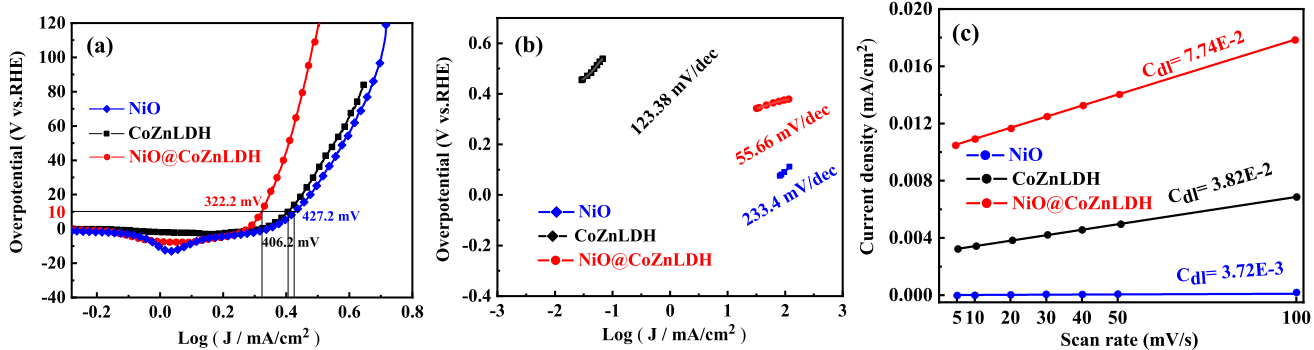


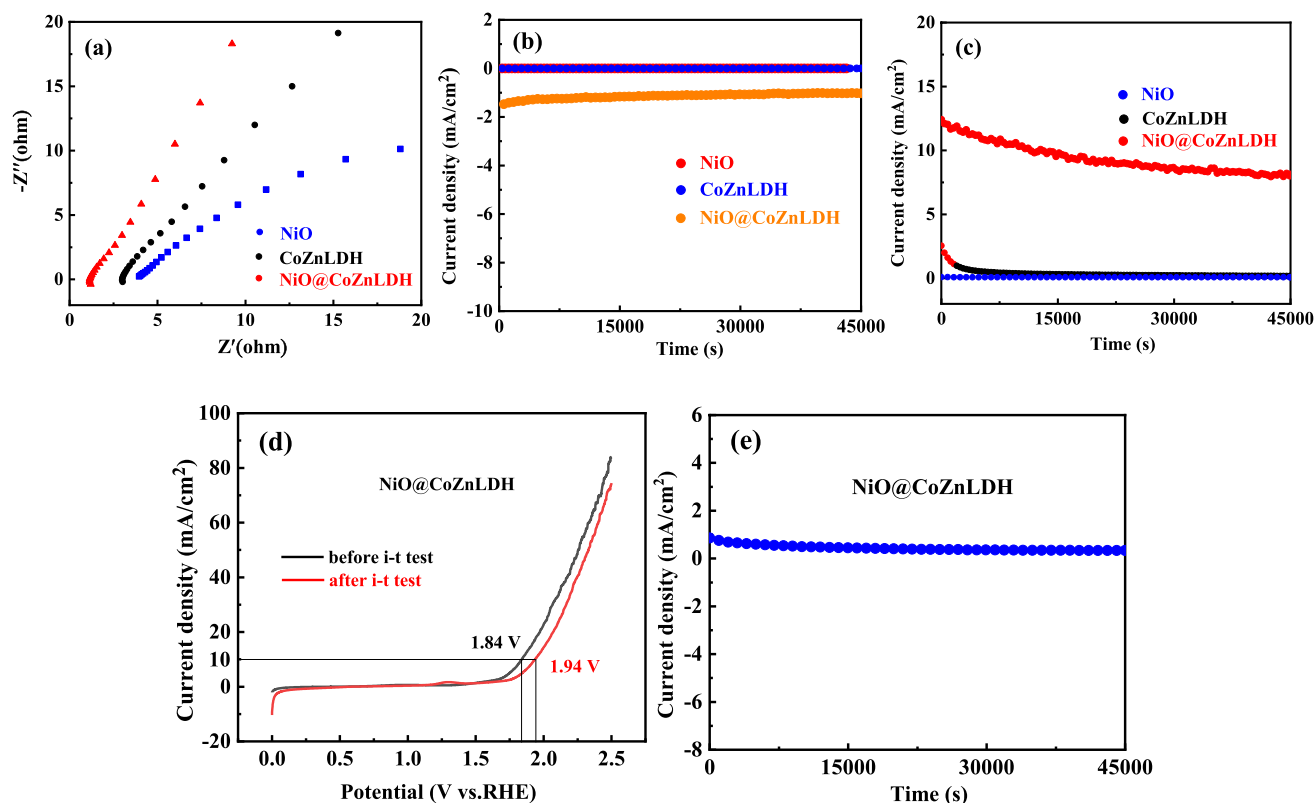
**Figure 8** OER performance of NiO, CoZnLDH, NiO@CoZnLDH **a** Comparison of LSV curve; **b** Comparison of Tafel slope; **c** Comparison of Cdl curves.

**Table 2** Comparison of OER performance of NiO@CoZnLDH electrocatalyst with other system catalysts

Materials	Overpotential (mV)	Electrolyte	Tafel plot (mV dec <sup>-1</sup> )	Refs
AVL-CuO-ZrO <sub>2</sub>	430	1 M KOH	116	[39]
AVL-CuO-Sb <sub>2</sub> O <sub>3</sub>	540	KOH	155	[47]
MgFe <sub>2</sub> O <sub>4</sub> nanospheres	1090	1 M KOH	317	[48]
Ni/NiS/NC	337	1 M KOH	52	[49]
N-NiMoO <sub>4</sub> /Ni/CNTs	330	1 M KOH	89.5	[50]
MnO <sub>2</sub> -Ni <sub>0.02(M)</sub>	445	0.1 M KOH	149	[51]
Au <sub>8.0</sub> @C/Co <sub>3</sub> O <sub>4</sub>	451	1 M KOH	74.7	[45]
CoFe-MnO <sub>2</sub> @TNTA	412	1 M KOH	69	[52]
NiO@CoZn-LDH	322.2	1 M KOH	55.66	This work

NiO@CoZnLDH electrode showed excellent electrocatalytic performance (Tables 1 and 2) [39–52]. Fig. 8c compares the Cd<sub>1</sub> values of the three electrodes. The NiO@CoZnLDH composite electrocatalyst achieves the highest Cd<sub>1</sub> value (0.0774 mF/cm<sup>2</sup>), surpassing those of NiO ( $3.72 \times 10^{-3}$  mF/cm<sup>2</sup>) and CoZnLDH (0.0382 mF/cm<sup>2</sup>), indicating a greater electrochemically active surface area and enhanced performance for the OER.

To investigate the electron transfer capability during water electrolysis, EIS was performed (Fig. 9a). The NiO@CoZnLDH electrode exhibited the steepest slope in the low-frequency region, indicating superior diffusion efficiency (i.e., lower diffusion resistance). Chronoamperometric curves for the HER and OER are shown in Figs. 9b, c, respectively, confirming the stability of all three electrocatalysts (NiO, CoZnLDH, NiO@CoZnLDH) during 43,200 s (12 h) of continuous operation. Furthermore, the overall water splitting capability was validated via LSV (Fig. 9d) and chronoamperometric tests (Fig. 9e). The system remained stable during the overall water splitting reaction at 1.84 V

**Figure 9** **a** EIS curves of NiO, CoZnLDH, NiO@CoZnLDH; **b** i-t curve of the HER reaction of NiO, CoZnLDH, NiO@CoZnLDH; **c** i-t curve of the OER reaction of NiO, CoZnLDH, NiO@

CoZnLDH; **d** LSV curves of complete water reaction of NiO@CoZnLDH; **e** i-t curve of the complete water reaction of NiO@CoZnLDH.

for 12 h, with minimal change in overpotential before and after the process at a current density of 10 mA/cm<sup>2</sup>, indicating excellent performance and durability for total water splitting.

**iR Compensation:** To eliminate the voltage drop caused by solution resistance (iR drop) and to ensure that the measured overpotential accurately reflects the intrinsic electrochemical behavior at the electrode–electrolyte interface, iR compensation was applied during the OER testing. The procedure was conducted as follows: a small-amplitude AC signal (10 mV) was applied near the open-circuit potential over a frequency range of 100 kHz–0.1 Hz to determine the uncompensated solution resistance ( $R_u$ ). The iR compensation level was set to 90% using the electrochemical workstation software. A scan rate of 5 mV/s was employed for the LSV measurement, and the iR-compensated polarization curve was subsequently recorded.

## Conclusion

In summary, the NiO@CoZnLDH composite was successfully synthesized via a scalable two-step hydrothermal method, demonstrating exceptional potential as a bifunctional electrocatalyst. The material exhibited outstanding performance in supercapacitor applications, with a high energy density of 9.44 Wh/kg, a power density of 1132 W/kg, and a long-term cycling stability of 73.6% capacitance retention after 8000 cycles, establishing it as a strong candidate for advanced energy storage devices. Additionally, its electrocatalytic activity in water electrolysis—reflected by low overpotentials for the hydrogen evolution reaction (188.8 mV) and oxygen evolution reaction (322.2 mV), along with stable operation over 12 h—underscores its suitability for sustainable hydrogen production. The synergistic integration of NiO and CoZnLDH phases is critical to enabling this dual functionality. These findings position NiO@CoZnLDH as a promising multifunctional material for energy storage and conversion technologies.

## Acknowledgements

This work was supported 2024 Fundamental Research Project (No. LJ212410154010) of the Educational

Department of Liaoning Province, Liaoning Provincial Natural Science Foundation PhD Startup Project (No. 2024-BS-242).

## Funding

2024 Fundamental Research Project of the Educational Department of Liaoning Province, No. LJ212410154010, Dong-Mei Ma, Liaoning Provincial Natural Science Foundation PhD Startup Project, No. 2024-BS-242,Xingming Zhao

## Declarations

**Conflict of interest** The authors declare that they have no known competing financial interests or personal relationships that could have appeared to influence the work reported in this paper.

**Supplementary Information** The online version contains supplementary material available at <https://doi.org/10.1007/s10853-025-11455-8>.

## References

- [1] Diao SK, Wang TW, Kuang W, Yan S, Zhang XT, Chen MX, Liu Y, Tan AD, Yang TR, Liu JG (2025) Highly durable porous NiO-derived electrodes with superior bifunctional activity for scalable alkaline water electrolysis. *Chem Eng J* 504:158738
- [2] Gao DH, Ji S, Linkov V, Wang RF (2022) High current water electrolysis catalyst based on Fe/Ni(Ni/Fe) hierarchically structured electrode. *Int J Hydrogen Energy* 47:37831–37839
- [3] Munawar T, Bashir A, Rafaqat M, Shen LS, Tu ZM, Zhi-ani M, Iqbal F, Yan CF (2025) Metal oxide/chalcogenide/hydroxide catalysts for water electrolysis. *Int J Hydrogen Energy* 141:823–869
- [4] Yue HL, Zeng HY, Ya W, Luo CW, Tian ZF, Xu KW (2025) Oxalate-derived NiO@NiAl-layered double hydroxide core-shell material for supercapacitors. *Appl Clay Sci* 267:107715
- [5] Mosaddegh F, Esfandian H, Lashkenari MS (2024) Synthesis of NiO/ZnO/GO nanocomposites derived from ni-zn-H<sub>2</sub>BDC metal–organic framework for

- high-performance supercapacitor electrodes. *Electrochim Acta* 502:144860
- [6] Acharyaa J, Park M, Ko TH, Kim BS (2021) Leaf-like integrated hierarchical  $\text{NiCo}_2\text{O}_4$  nanorods@Ni-Co-LDH nanosheets electrodes for high-rate asymmetric supercapacitors. *J Alloy Compd* 884:161165
- [7] Chatterjee DP, Nandi AK (2021) A review on the recent advances in hybrid supercapacitors. *J Mater Chem A* 9:15880–15918
- [8] Gao R, Zhu J, Yan DP (2021) Transition metal-based layered double hydroxides for photo(electro)chemical water splitting: a mini review. *Nanoscale* 13:13593–13603
- [9] Boumeriame H, Da Silva ES, Cherevan AS, Chafik T, Faria JL, Eder D (2022) Layered double hydroxide (LDH)-based materials: a mini-review on strategies to improve the performance for photocatalytic water splitting. *J Energy Chem* 64:406–431
- [10] Zhang Y, Hu S, Li CE, Yan XH, Zhang YY, Yin RB, Wei YF, Gao KZ, Gao HL (2025) Advanced strategies for enhancing electrochemical performance of NiAl LDH electrodes in supercapacitors. *Coordin Chem Rev* 531:216497
- [11] Du JJ, Zhou Y, Liu XH, Cui XX, Zhang X, Wang B, Feng X, Zhu J, Zuo H, Li Q, He XH, Hu P (2024) Rational design of porous vanadium-based alloys modified with a Ni-Cu-Mo coating for alkaline water electrolysis. *Electrochim Acta* 499:144676
- [12] Yang WD, Zhao RD, Guo FY, Xiang J, Loy S, Liu L, Dai JY, Wu FF (2023) Interface engineering of hybrid  $\text{ZnCo}_2\text{O}_4@\text{Ni}_2.5\text{Mo}_6\text{S}_{6.7}$  structures for flexible energy storage and alkaline water splitting. *Chem Eng J* 454:140458
- [13] Nawaz M, Mu YQ, Gao YY, Jiang SS, Liu XY, Tao R, Chu ZM, Fan XX, Xu C (2025) Development of Z-scheme al– $\text{SrTiO}_3/\text{g-C}_3\text{N}_4$  heterojunctions with Co-rhx/cr<sub>2-x</sub>O<sub>3</sub> co-catalysts for enhanced photocatalytic overall water splitting. *Int J Hydrogen Energy* 124:84–91
- [14] Xu YF, Lu WB, Xu GB, Chou TW (2021) Structural supercapacitor composites: A review. *Compos Sci Technol* 204:108636
- [15] Tundwal A, Kumar H, Binoj BJ, Sharma R, Kumar G, Kumari R, Dhayal A, Yadav A, Singh D, Kumarc P (2024) Developments in conducting polymer-, metal oxide-, and carbon nanotube-based composite electrode materials for supercapacitors: a review. *RSC Adv* 14:9406–9439
- [16] Xua JH, Wu L, Liu Y, Zhang JF, Liu JM, Shu SS, Kang X, Song QG, Liu D, Huang F, Hu Y (2020) NiO-rGO composite for supercapacitor electrode. *Surf Interfaces* 18:100420
- [17] Mulla MG, Pittala RK (2025) Fabrication and physico-chemical properties of nickel oxide (NiO) thin films. *Ceram Int* 51:22255–22265
- [18] Sethi M, Shenoy US, Bhat DK (2021) Simple solvothermal synthesis of porous graphene-NiO nanocomposites with high cyclic stability for supercapacitor application. *J Alloys Compd* 854:157190
- [19] Avinash B, Ravikumar CR, Anil Kumar MR, Santosh MS, Pratapkumar C, Nagaswarupa HP, Ananda Murthy HC, Deshmukh VV, Bhatt AS, Jahagirdar AA, Alam MW (2021) NiO bio-composite materials: photocatalytic, electrochemical and supercapacitor applications. *Appl Sur Sci Adv* 3:100049
- [20] Shah MZU, Feng J, BiBi F, Sajjad M, Qureshi MT, Shah A, Shah MS, Khaled AM, Salem MS (2025) Enhanced energy storage with  $\text{TiO}_2/\text{NiO}/\text{ZnO}$  core-shell heterostructures in hybrid battery-supercapacitor applications. *J Alloy Compd* 1013:178548
- [21] Yin HJ, Yuan K, Zheng YL, Sun XC, Zhang YW (2021) In situ synthesis of NiO/CuO nanosheet heterostructures rich in defects for efficient electrocatalytic oxygen evolution reaction. *J Phys Chem C* 125:16516–16523
- [22] Lei YT, Zhang LL, Zhou DN, Xiong CL, Zhao YF, Chen WX, Xiang X, Shang HS, Zhang B (2022) Construction of interconnected NiO/CoFe alloy nanosheets for overall water splitting. *Renew Energ* 194:459–468
- [23] Zeng ZF, Gao ZF, Guo ZC, Xu XW, Li Y, Lin L, Jia RP, Han S (2024) Anion substitution-induced CuCoSe hollow nanotubes as multifunctional electrode materials for supercapacitors and overall water splitting. *Fuel* 369:131769
- [24] Zheng F, Li X, Gaikwad MA, Jang SY, Kim JH (2023) FeOOH-induced electronic modulation of metal–organic framework-derived CoNi-ZLDH for overall water splitting. *Surf Interfaces* 42:103407
- [25] Wang J, Lv GC, Wang C (2021) A highly efficient and robust hybrid structure of CoNiN@NiFe LDH for overall water splitting by accelerating hydrogen evolution kinetics on NiFe LDH. *Appl Surf Sci* 570:151182
- [26] Yao HX, Wang ST, Cao YL, Chen RQ, Lu ZJ, Hu JD, Xie J, Hao AZ (2022) High-performance bifunctional electrocatalysts of CoFe-LDH/NiCo<sub>2</sub>O<sub>4</sub> heterostructure supported on nickel foam for effective overall water splitting. *J Alloy Compd* 926:166846
- [27] Song CY, Liu Y, Wang YC, Tang SH, Li WK, Li Q, Zeng J, Chen L, Peng HC, Lei YP (2021) Highly efficient oxygen evolution and stable water splitting by coupling NiFe LDH with metal phosphides. *SCMs* 64:1662–1670
- [28] Nie F, Li Z, Dai XP, Yin XL, Gan YH, Yang ZH, Wu BQ, Ren ZT, Cao YH, Song WY (2022) Interfacial electronic modulation on heterostructured NiSe@CoFe LDH nanoarrays for enhancing oxygen evolution reaction and water splitting by facilitating the deprotonation of OH to O. *Chem Eng J* 431:134080

- [29] Zhu FF, Liu WJ, Liu Y, Shi WD (2020) Construction of porous interface on CNTs@NiCo-LDH core-shell nanotube arrays for supercapacitor applications. *Chem Eng J* 383:123150
- [30] Chu HS, Ma DM, Wu FF, Zhao RD, Jun X, Li LF, Zhao XM, Wang TL (2025) ZnS@Co(OH)<sub>2</sub> nanostructured materials with high-performance energy storage and superior electrocatalytic activity. *Ceram Int* 51:17630–17640
- [31] Xia XH, Tu JP, Mai YJ, Chen R, Wang XL, Gu CH, Zhao XB (2011) Graphene sheet/porous NiO hybrid film for supercapacitor applications. *Chemistry* 17:10898–10905
- [32] Yang LJ, Zhao YJ, Zhun LJ, Xia DH (2023) Rational construction of grille structured P-CoZnO-Cu<sub>2</sub>SeS/NF composite electrocatalyst for boosting seawater electrolysis and corrosion resistance. *Appl Surf Sci* 631:157541
- [33] Thommes M, Kaneko K, Neimark AV, Olivier JP, Reinoso FR, Rouquerol J, Sing KSW (2015) Physisorption of gases, with special reference to the evaluation of surface area and pore size distribution (IUPAC technical report). *Pure Appl Chem* 87:1051–1069
- [34] Chu WJ, Shi ZJ, Hou YD, Ma DN, Bai X, Gao YF, Yang NJ (2020) Trifunctional of phosphorus-doped NiCo<sub>2</sub>O<sub>4</sub> nanowire materials for asymmetric supercapacitor, oxygen evolution reaction, and hydrogen evolution reaction. *ACS Appl Mater Interfaces* 12:2763–2772
- [35] Cottineau T, Toupin M, Delahaye T, Brousse T, Belanger D (2006) Nanostructured transition metal oxides for aqueous hybrid electrochemical supercapacitors. *Appl Phys A Mater Sci Process* 82:599–606
- [36] He Y, Chen W, Li X, Zhang Z, Fu J, Zhao C, Xie E (2013) Freestanding three-dimensional Graphene/MnO<sub>2</sub> composite networks as ultralight and flexible supercapacitor electrodes. *ACS Nano* 7:174–182
- [37] Wang Q, Wen Z, Li J (2006) A hybrid supercapacitor fabricated with a carbon nanotube cathode and a TiO<sub>2</sub>-B nanowire anode. *Adv Funct Mater* 16:2141–2146
- [38] Dubal DP, Gund GS, Lokhande CD, Holze R (2014) Controlled growth of CoS<sub>x</sub> nanostrip arrays (CoS<sub>x</sub>-NSA) on nickel foam for asymmetric supercapacitors. *Energy Technol-Ger* 2:401–408
- [39] Azhar S, Ahmad KS, Abrahams I, Lin W, Gupta R, El-marghany A (2023) Synthesis of phyto-mediated CuO-ZrO<sub>2</sub> nanocomposite and investigation of their role as electrode material for supercapacitor and water splitting studies. *J Mater Res* 38:4937–4950
- [40] Amiri M, Afruz A, Nozari-Asbemarz M, Bezaatpour A, Vocke H, Taffa DH, Wark M (2023) Overall water splitting by bio-modification of Fe<sub>3</sub>O<sub>4</sub> with Co-Ni complexes. *J Electrochim Soc* 170:84511
- [41] Wei GJ, He J, Zhang WQ, Zhao XX, Qiu SJ, An CH (2018) Rational design of co(II) dominant and oxygen vacancy defective CuCo<sub>2</sub>O<sub>4</sub>@CQDs hollow spheres for enhanced overall water splitting and supercapacitor performance. *Inorg Chem* 57:7380–7389
- [42] Shit S, Chhetri S, Jang W, Murmu N, Koo H, Samanta P, Kuila T (2018) Cobalt sulfide/Nickel sulfide heterostructure directly grown on Nickel foam: an efficient and durable electrocatalyst for overall water splitting application. *ACS Appl Mater Interfaces* 10:27712–27722
- [43] Barik S, Kharabe GP, Illatvalappil R, Singh CP, Kanheerampockil F, Walko P, Bhat S, Devi RN, Vinod CP, Krishnamurty S, Kurungot S (2023) Active Site Engineering and Theoretical Aspects of “Superhydrophilic” Nanostructure Array Enabling Efficient Overall Water Electrolysis. *Small* 19:2304143
- [44] Zou XX, Huang XX, Goswami A, Silva R, Sathe B, Mikmekova E, Asefa T (2014) Cobalt-embedded nitrogen-rich carbon nanotubes efficiently catalyze hydrogen evolution reaction at all pH values. *Angew Chem* 126:4461–4465
- [45] Gujjula SR, Karingula S, Shahjahan S, Siliveri S, Goskula S, Chirra S, Gobi KV, Narayanan V (2023) Rational design of metal organic framework derived porous Au@Co<sub>3</sub>O<sub>4</sub>/C nanocomposite materials for the electrochemical overall water splitting. *J Mater Sci* 58:9130–9147
- [46] Ren C, Chen YJ, Du LZ, Wang Q, Li LG, Tian GH (2021) Hierarchical CuCo<sub>2</sub>S<sub>4</sub> nanoflake arrays grown on carbon cloth: a remarkable bifunctional electrocatalyst for overall water splitting. *ChemElectroChem* 8:1134–1140
- [47] Azhar S, Ahmad KS, Andleeb S, Abrahams I, Lin W, Gupta R, El-marghany A (2024) Phyto-mediated CuO-Sb<sub>2</sub>O<sub>3</sub> nanocomposite supported on Ni foam as a proficient dual-functional supercapacitor electrode and overall water splitting electrocatalyst. *J Electrochim Soc* 54:963–976
- [48] Maitra S, Mitra R, Nath TK (2021) Investigation of electrochemical performance of sol-gel derived MgFe<sub>2</sub>O<sub>4</sub> nanospheres as aqueous supercapacitor electrode and bi-functional water splitting electrocatalyst in alkaline medium. *Curr Appl Phys* 27:73–88
- [49] Ding JT, Ji S, Wang H, Gai HJ, Liu FS, linkov V, Wang RF (2019) Mesoporous nickel-sulfide/nickel/ N-doped carbon as HER and OER bifunctional electrocatalyst for water electrolysis. *Int J Hydrogen Energy* 44:2832–2840
- [50] Li GL, Qiao XY, Miao YY, Wang TY, Deng F (2023) Synergistic effect of N-NiMoO<sub>4</sub>/Ni heterogeneous interface with oxygen vacancies in N-NiMoO<sub>4</sub>/Ni/CNTs for superior overall water splitting. *Small* 19:2207196
- [51] Bera K, Karmaker A, Karthick K, Sankar SS, Kumaravel S, Madhu R, Kundu S (2021) Enhancement of the OER kinetics of the less-explored  $\alpha$ -MnO<sub>2</sub> via nickel

- doping approaches in alkaline medium. Inorg Chem 60:19429–19439
- [52] Yang MY, Wang XX, Xu XW, Li YJ, Liu Y, Zhao JJ (2025) Facile preparation of CoFe-MnO<sub>2</sub>@titania nanotube array bifunctional electrodes for high-current-density water splitting at industrial temperatures. J Mater Sci Technol 211:123–133

**Publisher's Note** Springer Nature remains neutral with regard to jurisdictional claims in published maps and institutional affiliations.

Springer Nature or its licensor (e.g. a society or other partner) holds exclusive rights to this article under a publishing agreement with the author(s) or other rightsholder(s); author self-archiving of the accepted manuscript version of this article is solely governed by the terms of such publishing agreement and applicable law.